frontiers | Frontiers in Earth Science

TYPE Original Research
PUBLISHED 19 January 2023
DOI 10.3389/feart.2022.1084213

OPEN ACCESS

EDITED BY
Jilei Li,
Institute of Geology and Geophysics (CAS), China

REVIEWED BY
J. ZhangZhou,
Zhejiang University, China
Chunqing Sun,
Institute of Geology and Geophysics (CAS), China

*CORRESPONDENCE
Yigang Zhang,
zhangyigang@ucas.ac.cn
Dongdong Ni,
ddni@must.edu.mo

SPECIALTY SECTION
This article was submitted to Geochemistry, a section of the journal Frontiers in Earth Science

RECEIVED 30 October 2022
ACCEPTED 29 November 2022
PUBLISHED 19 January 2023

CITATION
Zhao Y, Zhang Y and Ni D (2023), Dynamic evolution of changbaishan volcanism in Northeast China illuminated by machine learning. *Front. Earth Sci.* 10:1084213. doi: 10.3389/feart.2022.1084213

Dynamic evolution of changbaishan volcanism in Northeast China illuminated by machine learning

Yong Zhao[1,2], Yigang Zhang[3]* and Dongdong Ni[1,2]*

[1]State Key Laboratory of Lunar and Planetary Sciences, Macau University of Science and Technology, Macau, China, [2]CNSA Macau Center for Space Exploration and Science, Macau, China, [3]Key Laboratory of Computational Geodynamics, College of Earth and Planetary Sciences, University of Chinese Academy of Sciences, Beijing, China

Previous studies propose that there is a mantle upwelling that generated the Cenozoic basalts in Changbaishan. However, the dominant source and mechanism of the mantle upwelling remains highly debated. Here we apply machine learning algorithms of Random Forest and Deep Neural Network to train models using global island arc and ocean island basalts data. The trained models predict that Changbaishan basalts are highly influenced by slab-derived fluid. More importantly, the fluid effect decreases with no $(^{87}Sr/^{86}Sr)_0$ and $\varepsilon_{Nd(t)}$ changes between 5 Ma and 1 Ma, then enhances with increasing $\varepsilon_{Nd(t)}$ and decreasing $(^{87}Sr/^{86}Sr)_0$ after 1 Ma. We propose that a gap opened at about 5 Ma and the hot sub-slab oceanic asthenosphere rose through the gap after 1 Ma, generating the basalts enriched in fluid mobile elements and with the addition of depleted mantle component derived from the sub-slab oceanic asthenosphere.

KEYWORDS

basalts, Northeast China, changbaishan, machine learning, subduction, fluid activity, stagnant slab

Introduction

In Northeast China, the late Cenozoic intraplate volcanic basalts are widely distributed. The Changbaishan (CBS) volcanic region, about 1300 km west of the Japan Trench and located on the border between China and North Korea, is the largest active magmatic center in Northeast China and covers an area of ca. 12,000 km^2 (Figure 1B). It mainly consists of CBS, Wangtian'e and Namphothe volcanoes. The start of volcanic activities in the CBS area occurred approximately in Miocene period and with several eruptions during the past 2,000 years including one of the largest recorded eruptions worldwide which occurred in approximately 946 AD and is called "Millennium Eruption" (Wei et al., 2003; Wei et al., 2013; Liu et al., 2015a). Seismic tomography images that the Pacific Plate penetrates the mantle at the Japan Trench (Figure 1A) and stagnates in the mantle transition zone (MTZ; Figure 1C) beneath Northeast China (Huang and Zhao, 2006; Fukao et al., 2009; Zhao et al., 2009; Obayashi et al., 2013; Tang et al., 2014).

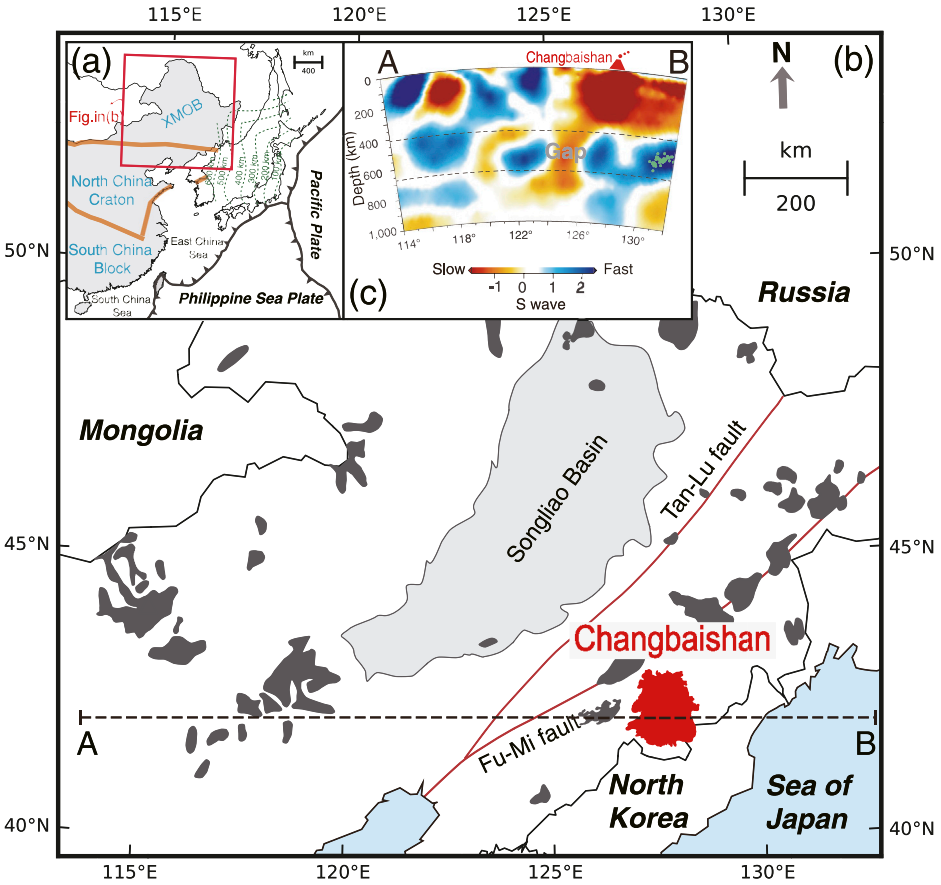

FIGURE 1
(A) Simplified geological map showing the spatial distribution of tectonic plates in East Asia. Green dashed lines indicate the Wadati-Benioff zone, showing the depths of subducted Pacific slab (Tang et al., 2014). **(B)** Distributions of Cenozoic basalts (dark grey patches, the Changbaishan volcanic filed with red shadow) and deep faults (red lines) in northeastern China after Liu et al. (2001). The dashed line indicates location of the cross-section for **(C)**. **(C)** Vertical cross-section of S-wave velocity tomography under northeast Asia, modified from Tang et al. (2014). Green dots are deep earthquakes from 1973 to 2012. XMOB is the Xing'an Mongolia Orogenic Belt. **(B)** is an enlarged view of the red box in **(A)**.

Previous studies have proposed that the mantle upwelling is the cause of the generation of Cenozoic basalts in Northeast China (Zou et al., 2008; Zhao et al., 2009; Tang et al., 2014; Wang et al., 2015; Tian et al., 2016). The mantle upwelling ascends to shallow levels and results in the widely intraplate volcanism in northeast China. However, the source and mechanism of the mantle upwelling remains highly debated. From seismological studies, Zhao et al. (2009), using high-resolution tomography of the upper mantle under the CBS volcanic area, proposed that deep dehydration of the stagnant slab leads to the upwelling, forming the active intraplate volcanoes in Northeast China. Recently, Tian et al. (2016) applied a receiver-function method to study the MTZ structure beneath the CBS and suggested that the CBS volcanoes are fed by the fluid released from subducting slab. However, Tang et al. (2014) identified an anomaly in the stagnant Pacific slab using seismic tomography analysis (Figure 1C). They considered it as a gap in the stagnant slab through which the mantle upwelling from just below the 660-km discontinuity could pass.

From the geochemical studies, there exist also great controversies as to whether the mantle upwelling originates from the top of the stagnant slab or the lower mantle. For example, Kuritani et al. (2011) attributed the high Ba/Th ratio and EM1-like (enriched mantle-1: Zindler and Hart, 1986) signature of the volcanoes around CBS to the involvement of stagnant slab-derived materials. The low δ^{26}Mg and high δ^{66}Zn anomaly in eastern China are suggested to reflect the addition of recycled slab materials in the mantle sources (Liu et al., 2016a; Li et al., 2017). Furthermore, the contribution of slab dehydration is supported by the finding of high-water content for the source mantle of the basalts (Kuritani et al., 2019; Di et al., 2020). Recently, Zhao et al. (2019) found that most Cenozoic basalts in Northeast China are influenced by the fluid released from the stagnant slab using machine learning method. However, some studies, such as significant ^{230}Th excesses in basalts from the CBS (Zou et al., 2008), argue against melting of the mantle by the addition of fluid.

In this study, the geochemical compositions of the CBS basalts are analyzed in a more comprehensive way, compared with specific traditional geochemical indicators, to obtain a more exhaustive understanding of its genesis. Machine learning algorithms, including Deep Neural Network (DNN) and Random Forest (RF), which use major and trace element compositions, are applied to predict the degree of influence of water in the genesis of the Cenozoic basalts in CBS volcanoes. RF and DNN methods can detect patterns in high dimensional data and make predictions in complex situations (Breiman, 2001; LeCun et al., 2015). To establish the predicting models, training data are taken from GEOROC database (GEOROC, 2015) for global island arc basalts (IAB) and ocean island basalts (OIB), based on the datasets in Zhao et al. (2019). The dominant geochemical features of the IAB and OIB data, extracted by RF and Principal Component Analysis (PCA), indicate the opposite ways the basalts are influenced by slab-derived fluid, with IAB enriched in fluid mobile elements and OIB in fluid immobile elements. Thence, the trained RF and DNN models are used to inform how the time series Cenozoic basalts in CBS are influenced by the slab-derived fluid during their generations. The predicting results are further compared with the temporal variations of strontium (Sr) and neodymium (Nd) isotopes. All these give us information on the source and mechanism of the mantle upwelling in generating the Cenozoic CBS basalts.

Methods and data

Machine learning approaches

RF is a forest consisting of many decision trees (Breiman, 2001). A decision tree is a series of nodes, a directional graph that starts at the base with a single root node and extends to many leaf nodes that represent the class that the tree can classify. To generate each node in the tree, the training dataset that arrives at a node is split into two subsets based on a certain feature from the dataset. Decisions of the tree are generated until the tree has reached a maximum depth or the number of data points at a node has reached a minimum size. The creation of decisions is made on training dataset. When a new point from the testing dataset falls on a leaf, following a path of decisions in the trained tree, it is given the class by majority vote. A random forest is an ensemble of decision trees given by a bootstrap resampling of the training dataset. Bootstrap resampling (Breiman et al., 1999) is used to reduce the variance of a decision tree. The idea is to create several subsets of data from training dataset chosen randomly with replacement. To build a node, the set of features is also chosen randomly. In a classification problem, each tree votes and the most popular class is chosen as the last result. A simple description of the random forest training procedure is summarized in the following: 1) data pre-processing; 2) at the current node, randomly select a subset of features form the available features. The number of selected features is usually much smaller than the total number of available features; 3) compute the best split point for each tree that partitions the data into two daughter nodes that are maximally dissimilar to each other and reduce the number of available features from this node on; 4) repeat steps 1 to 3 for each tree in the forest, generating the entire tree structure; 5) vote on the output of each tree in the forest. Hyper-parameters, including the number of trees as well as features to consider when looking for the best split and the minimum number of samples required to split an internal node, are tuned by grid search based on a 10-fold cross-validation. In a 10-fold cross-validation, the original data is randomly divided into 10 equal sized subsamples. Of the 10 sub-samples, a single sub-samples is retained as the validation data for testing the classification, which is trained by using the union of the remaining nine subsamples. The cross-validation process is then repeated 10 times, with each repetition changing the test subsamples to obtain 10 independent estimates of the accuracy of the discrimination approaches.

DNN inspired by the way biological neurons process information is a network structure composed of multiple processing layers, including one input layer, several hidden layers, and one output layer (LeCun et al., 2015). The connections between layers are called “weights.” During the training of a model, the scaled input data is passed through the constructed neural network structure and the outputs are computed. The cross-entropy (Shore and Johnson, 1980) method is used to compute the difference (error) between network outputs and real targets. Then, the errors are propagated from the output end to the input layer and the weights of the network are adjusted to make sure that the errors would be reduced in the next iteration. In other words, the computed outputs become closer to the real ones. The 10-fold cross-validation is also used to find the optimal DNN model. In this study, rectified linear units (ReLU) activation function for the hidden layers and softmax activation function for output layer are used. In the process of training, we use adaptive moment estimation (Adam) optimizer (Kingma and Ba, 2014), which is regarded as robust to the choice of hyper-parameters (Goodfellow et al., 2016). To prevent neural networks from overfitting which simply means that the trained model doesn’t generalize well from training data to unseen data, early stopping and dropout (Srivastava et al., 2014) techniques are applied to DNN model. When using early stopping, we monitor testing loss and training stops when loss is no longer falling within a few epochs. Dropout is applied to all hidden layers with the probability of 0.1. The weights before learning stars are initialized randomly.

PCA is a statistical procedure that is often used when initially extracting what’s underneath the hood of your data from a high-

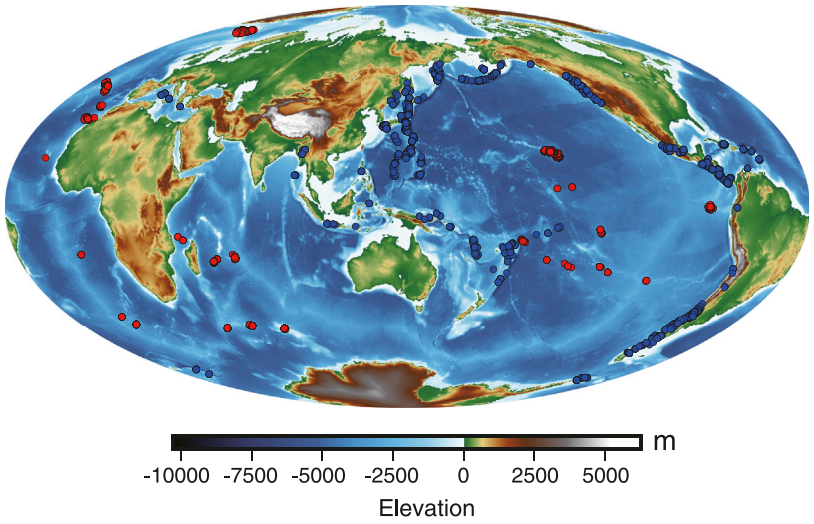

FIGURE 2
Geological map showing the locations of IAB (blue circles) and OIB (red circles) samples used during this study. Map created with open source PyGMT Python module (Uieda et al., 2021).

dimensional space by projecting it into a lower-dimensional sub-space. Important features in the data could be revealed in this sub-space.

In this study, DNN and RF are used to build classification models for predicting the CBS basalts. Compared with the "blackbox" features of DNN, RF model is interpretable and can give the importance of features during classification, that is, which elements are critical in discriminating one class from another. The importance of a feature is measured by the mean decrease in impurity (MDI), which is the average decrease in impurity of the data when this feature is dropped. The larger the decrease, the more important the feature is. MDI calculates each feature importance as the sum over the number of splits that include the feature, proportionally to the number of samples it splits (Louppe et al., 2013). After MDI is calculated, the importance of individual elements for IAB and OIB can be computed as follows:

$$\mathbf{I}_{ij} = \boldsymbol{MDI}(j)^{*}\frac{\sum_{m}^{N_i}\boldsymbol{s}(i)_{mj}}{\boldsymbol{N_i}}$$

with i ∈{IAB, OIB}, j an element, N_i the number of samples for one class, and $s(i)_{mj}$ the value of input matrix for one class. PCA is used for extracting geochemical features of IAB and OIB. A consistency of the important features extracted from RF and PCA permits a liaison of the classification with important features. The important features are analyzed to give the geological process that dominates the formation of the classified basalts.

RF and DNN models are trained on NVIDIA GeFore GT 730 graphics card using the open source Scikit-learn (Pedregosa et al., 2011) and Keras (Chollet, 2015) Python module respectively.

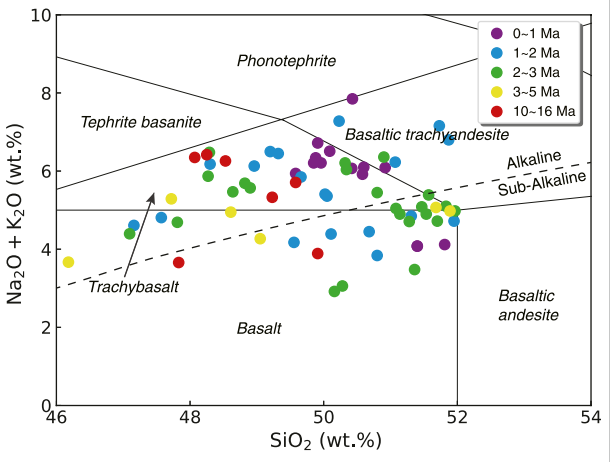

FIGURE 3
Total alkalis vs. SiO_2 diagram (Middlemost, 1994) for classification of the Cenozoic basalts in CBS volcanoes, which are from Zhang et al. (2018) and Yu et al. (2018).

Training and prediction data sets

Here the basalt whole-rock compositional data from GEOROC geochemical database in February 2019, with a total

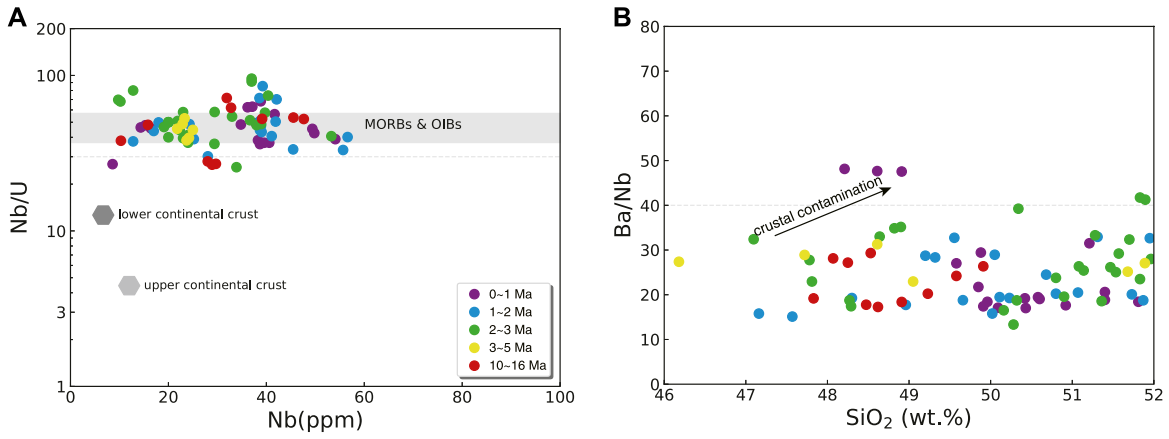

FIGURE 4
(A) Nb/U vs. Nb. **(B)** Ba/Nb vs. SiO_2. In **(A)**, the gray area is Nb/U of mid-ocean ridge basalts (MORBs) and ocean island basalts (OIBs) (Hofmann et al., 1986). Data for the upper continental crust and lower continental crust is from Rudnick and Gao (2014). The arrow in **(B)** indicates a crustal contamination trend.

of 51,327 island arc and 43,629 ocean island rock samples, are used to build our DNN and RF models.

Following Zhao et al. (2019), additional data pre-processing procedures are necessary before building machine learning models, which is to produce a suitably "clean" dataset. After data cleaning, a total of 1,966 IAB and 1,798 OIB samples with complete major elements (SiO_2, TiO_2, Al_2O_3, FeO^T, CaO, MgO, MnO, K_2O, Na_2O, and P_2O_5) and selected trace elements (Rb, Sr, Nb, Ba, La, Ce, Nd, Yb, Ta, Th, and U) are selected. The clean datasets are the same as Zhao et al. (2019). The locations of the selected samples are shown in Figure 2.

The Cenozoic basalts in CBS area are extracted from Zhang et al. (2018) and Yu et al. (2018), originally 385 in number and 79 after data pre-processing from Zhao et al. (2019). These samples are from CBS, Wangtian'e and Namphothe volcanoes and primarily alkaline basalts (Figure 3). These basalts erupted in three stages based on radiometric dating results and field observations (Liu et al., 2015a): pre-shield stage (ca. 23–10 Ma), shield-forming stage (ca. 5–1 Ma) and post-shield stage (ca. 1–0 Ma). The basalts with age of 0.001 Ma are youngest among these cleaned samples. There is currently no proper explanation for the emergence of an eruption gap between pre-shield stage and shield-forming stage owing to the few outcrops of pre-shield basalts (Zhang et al., 2018). It is noteworthy that most samples are not significantly contaminated by continental crust (Figure 4). The continental crust is characterized by low Nb/U ratios; however, these samples have high Nb/U (30–100), falling primarily into the range of MORBs and OIBs (Figure 4A). Furthermore, due to the fact that the continental crust is enriched in Ba relative to Nb (Rudnick and Gao, 2014), if crustal contamination had occurred, Ba/Nb ratios would have shown a positive correlation with SiO_2, which was not observed in these samples (Figure 4B). These samples with Nb/U < 30 or Ba/Nb > 40 may experience crustal contamination and is excluded from our study. Finally, 69 time series samples are fed into the well-trained machine learning models to predict the variation of fluid activity over time.

Data standardization

Standardization of data sets is a common requirement before the use of machine learning methods. Igneous rocks have wide variations in trace element concentrations, which can introduce bias and increase computational expense in the machine learning training process. In order to correctly and fully obtain information from high-dimensional geochemical data, centered log ratio (CLR) transformation (Aitchison, 1986) is used before the application of RF, DNN and PCA. Given sample $S = (x_1, x_2, ..., x_N)$, where x_i is the percentage of the ith element, the transformed sample can be expressed as follows:

$$S^* = \left(ln \frac{x_1}{g}, ln \frac{x_2}{g}, ..., ln \frac{x_N}{g} \right)$$

where g, the geometric mean of sample, can be calculated as:

$$g = \sqrt[N]{x_1^* x_2^* ... * x_N}$$

The transformed compositional datasets are followed by zero-mean normalization. RF, DNN, and PCA are then applied.

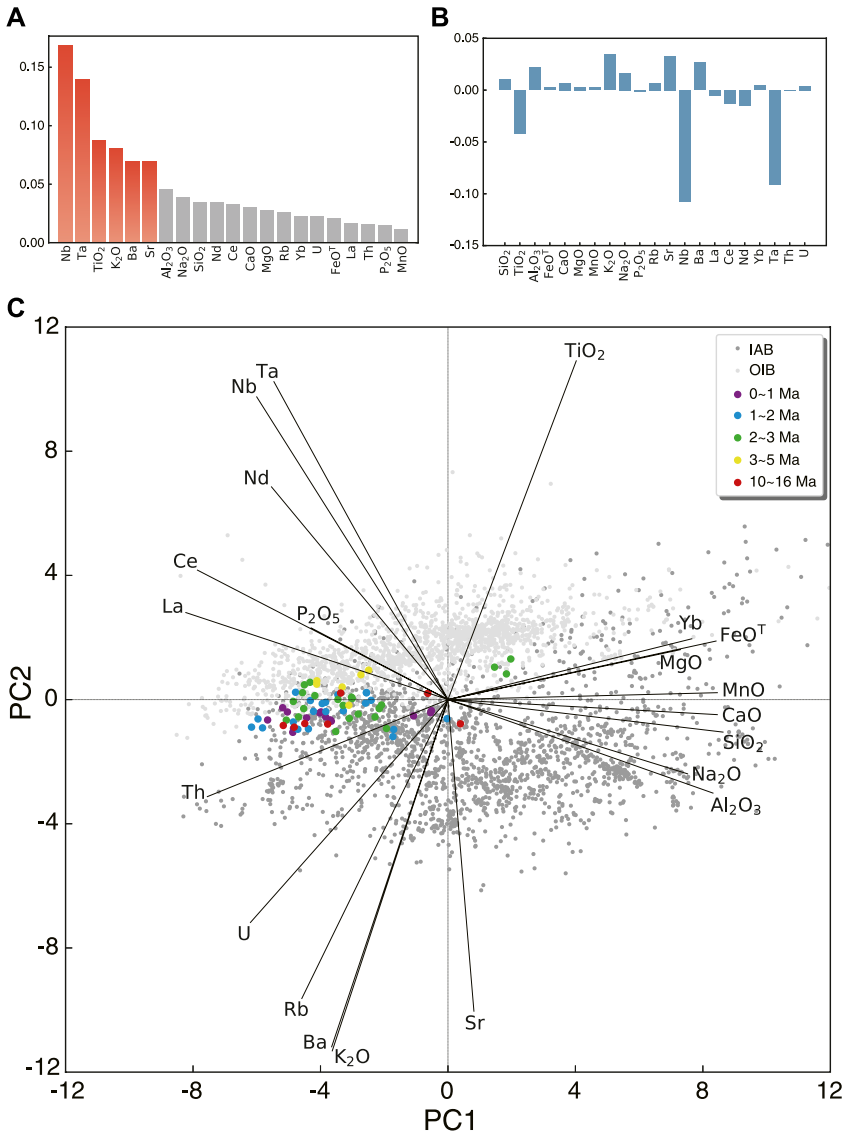

FIGURE 5
(A,B) Feature importance extracted from RF method after Zhao et al. (2019). **(C)** Compositional biplot of basalts from the CBS area, island arc and ocean island according to Zhao et al. (2019). Black lines mean the PC loadings for each element. A relatively large value signifies a large contribution of the element to the corresponding principal component. PC is principal component.

Results and discussion

Dominant geochemical features of the island arc basalts and ocean island basalts data from random forest and principal component analysis

In Figure 5A, Nb, Ta, TiO_2, K_2O, Ba and Sr are the most important classifiers used by the trained RF model to discriminate IAB and OIB. For IAB, Figure 5B shows positive loadings of K_2O, Ba, and Sr, which are highly fluid-mobile during subduction, and negative loadings of Nb, Ta, and TiO_2, which are fluid-immobile during subduction (McCulloch and Gamble, 1991; Pearce and Peate, 1995). Because our model is a binary classification, the trend for OIB is the reverse of that for IAB. Obviously, the dominant geochemical features of IAB and OIB are that IAB is enriched in highly fluid-mobile elements brought by fluid released from subducting slab and OIB is enriched in fluid-immobile elements coming from residue components of the fluid activity. A machine learning model trained using IAB and OIB data can thus tell us how the basalt has been influenced by subduction process and, in particular, whether it is influenced by the addition of the slab-derived fluid components.

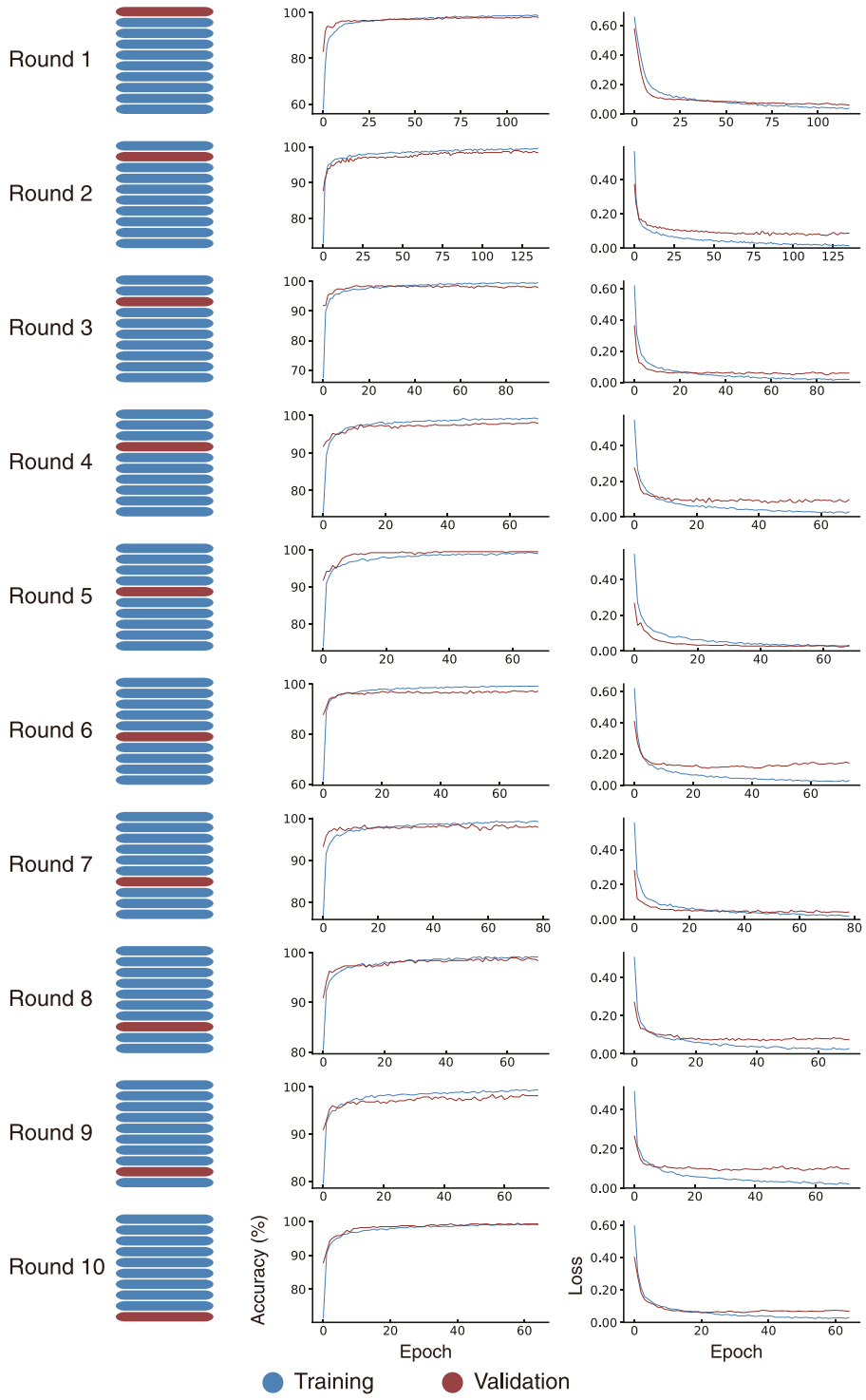

FIGURE 6
The DNN model accuracies and losses on training and testing sets for each epoch in the 10-fold cross-validation procedure. The accuracy and loss reach an approximate constant for both the training and testing data.

Similar results are also observed from PCA. As shown in Figure 5C, IAB and OIB are well distinguished in the direction of the second principal component (PC2) featured by large negative loadings of K_2O, Ba, and Sr on the negative side of PC2 for IAB and large positive loadings of Nb, Ta, and TiO_2 on the positive side of PC2 for OIB.

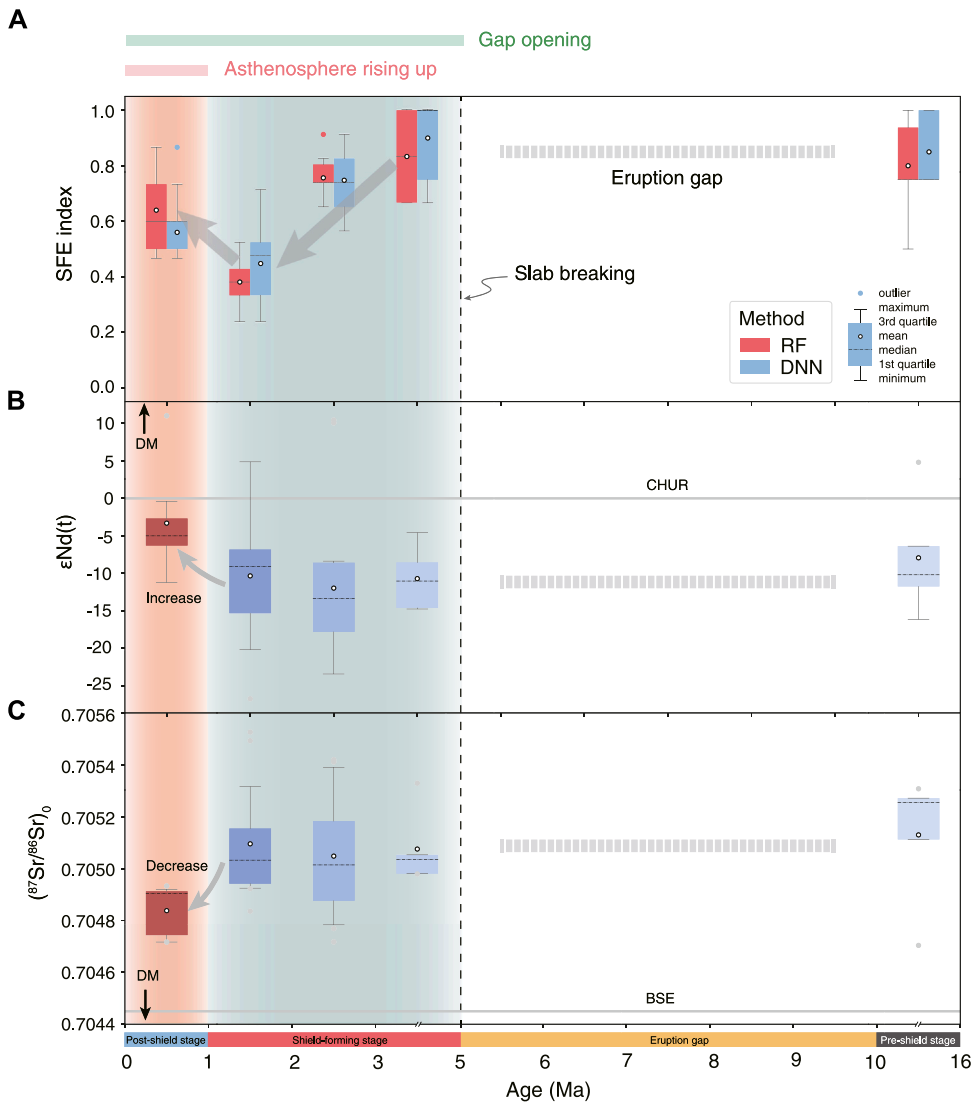

FIGURE 7
(A) The predictions of the RF and DNN models for basalts' SFE index in the Changbaishan. **(B,C)** Nd and Sr isotopic compositional variations with time for the Changbaishan basalts of 16–0 Ma ages. The increase of $\varepsilon_{Nd(t)}$ and decrease of $(^{87}Sr/^{86}Sr)_0$ (initial ratio) after 1 Ma indicate a more depleted mantle component is added to the source of the Changbaishan basalts. SFE, subduction fluid enrichment; CHUR, chondritic unfractionated reservoir; DM, depleted mantle; BSE, bulk silicate Earth.

Therefore, IAB is hereafter labeled as "subduction fluid enrichment" (SFE) and OIB as "no subduction fluid enrichment" (NSFE) in the subsequent establishment of RF and DNN models (Zhao et al., 2019).

In the direction of first principal component (PC1), high variability of IAB, OIB, and the Cenozoic basalts in CBS is seen, which might be the results of melting, crystallization, and fractionation of several minerals such as olivine, amphibole, and garnet and their complex combinations (Brandmeier & Wörner, 2016; Zhao et al., 2019).

Machine learning modeling

The input data are geochemical compositions of 10 oxides and 11 trace elements of rock samples. The target output is SFE or NSFE. Both machine learning models perform very well. We have re-optimized the hyper-parameters on the basis of the machine learning models of Zhao et al. (2019). For RF model, a tree number of 22 and a feature number of four when looking for the best split are used, and the resultant mean validation accuracy is 94.11%. The DNN model is the same as the model constructed in the previous study (Zhao et al., 2019). Tenfold

cross validation (Kohavi, 1995) shows that an average accuracy of 98.33% is achieved by the DNN model (Figure 6).

In order to evaluate whether the training datasets, that are IAB and OIB, are sufficient to obtain machine learning models with good performance, we trained three additional machine learning models with different sizes of training datasets, and the number of samples for label SFE or NSFE is 500, 1,000, and 1,500. We find that the accuracy of RF and DNN has reached 93.5% and 97.7% when the size of the training data set is 500, while the accuracy will increase by less than 0.5% if the sample size continues to increase. Therefore, the current size of the training data set (1,966 IAB and 1,798 OIB samples) is sufficient for machine learning models with excellent performances.

Predictions and isotopic features of the cenozoic basalts in changbaishan

A total of 69 basalt samples with ages from 15.1 to 0.001 Ma, divided into five age groups, are used to predict the influence of fluid released from the stagnant Pacific slab. After the prediction is completed, for each age group, we calculate the SFE index which is defined as follows:

$$\textbf{SFE index} = \frac{\textbf{SFE percentage} - \textbf{0.5}}{\textbf{0.5}}$$

with SFE percentage being the proportion of samples predicted by machine learning models as SFE for one age group (Zhao et al., 2019). A positive SFE index indicates addition of slab-derived fluid-mobile elements is dominant in basalts of one age group and a negative SFE index indicates the influence of fluid released from the slab is minor.

As shown in Figure 7A, predictions of the DNN and RF models are highly consistent, which indicates that different machine learning algorithms, representing different mappings from inputs to outputs, could decipher the same geochemical characteristics of the input data and give similar predictions. It is worth noting that the time-varying fluid activity trends of CBS basalts, predicted by the machine learning models trained with different sizes of training datasets, are basically consistent. As for PCA, it is not used to classify the Cenozoic basalts in CBS, but to extract the dominant geochemical features of IAB and OIB. As Figure 5C shows that most basalts in CBS are distributed on the IAB side, which is in general agreement with machine learning models results shown in Figure 7A. However, the temporal variation of SFE index from 5 to 1 Ma is not seen in the PC2. The divergence may be that only one dimension (PC2) is used in the PCA classification, which brings tremendous loss of information from other dimensions compared with the use of whole information in classifications by the RF and the DNN. Therefore, the RF and the DNN are preferable in making classifications.

Figure 7A shows that the CBS basalts have the positive SFE index and are thus largely influenced by the fluid released from the stagnant slab in the MTZ as the feature importance of the RF and PC2 of PCA reveals (Figure 5), which is supported by traditional seismological and geochemical observations (Zhao et al., 2009; Kuritani et al., 2011; Choi et al., 2020; Han et al., 2020; Li et al., 2020). From 5 to 1 Ma, the younger the basalts were, the weaker the influence of the stagnant slab was. After 1 Ma, the influence of fluid released from stagnant slab increased, which suggests a process provided additional slab-derived fluid. The influence of fluid for basalts older than 10 Ma (pre-shield stage) remained strong with a high SFE index and the effect of slab-derived fluid basically keep unchanged before and after the eruption gap (10–5 Ma). For the young basalts erupted after 1 Ma, the water content of the primary magma is estimated to be 1.2–1.8 wt% using thermodynamic analyses and mineral melt inclusions (Kuritani et al., 2019), which is consistent with the strong influence of slab-derived fluid determined by machine learning models. For the other basalts older than 1 Ma, due to the lack of studies on the water and slab fluid of primary magmas, the fluid activity that evolved over time could not be inferred though traditional geochemical methods.

Plots of basalt ages against whole-rock $\varepsilon_{Nd(t)}$ and $(^{87}Sr/^{86}Sr)_0$ (initial ratio) values (Figures 7B,C) show that these values are basically unchanged for basalts from 16 to 10 Ma and 5 to 1 Ma (pre-shield and shield-forming stages) with an average $\varepsilon_{Nd(t)}$ = −7.9 to −12.9 and average $(^{87}Sr/^{86}Sr)_0$ = 0.70504–0.70513. In contrast, basalts formed after 1 Ma have relatively higher average $\varepsilon_{Nd(t)}$ = −3 and lower average $(^{87}Sr/^{86}Sr)_0$ = 0.70484, indicating the addition of a relatively depleted mantle component to the source of the CBS basalts.

One possible process resulting in the addition of slab-derived fluid is a deep mantle plume heating to the stagnant slab in the MTZ. However, mantle tomography does not detect the trace of a deep mantle plume rooted from the core-mantle boundary (Zhao et al., 2009), which is supported by low $^3He/^4He$ ratios of the CBS hydrothermal fluids (Zhang et al., 2018) and ultramafic xenoliths (Chen et al., 2007). Another possible process is the contribution of oceanic asthenosphere beneath the stagnant Pacific slab. Globally observed seismic anisotropy has inferred the existence of asthenosphere flow parallel to the direction of subducting lithosphere (Long and Silver, 2008; Song and Kawakatsu, 2012). Numerical modelling and laboratory experiments suggest that the hot entrained oceanic asthenosphere could be transported and dragged down by subducting lithosphere to as deep as the lower mantle (Honda et al., 2007; Phipps Morgan et al., 2007; Morishige et al., 2010; Liu and Zhou, 2015). The MTZ beneath Northeast China, moreover, is particularly hydrous (Kelbert et al., 2009; Guo and Yoshino, 2013), with as much as ~1 wt% water (Karato, 2011), which could make local melting easier. In addition, the

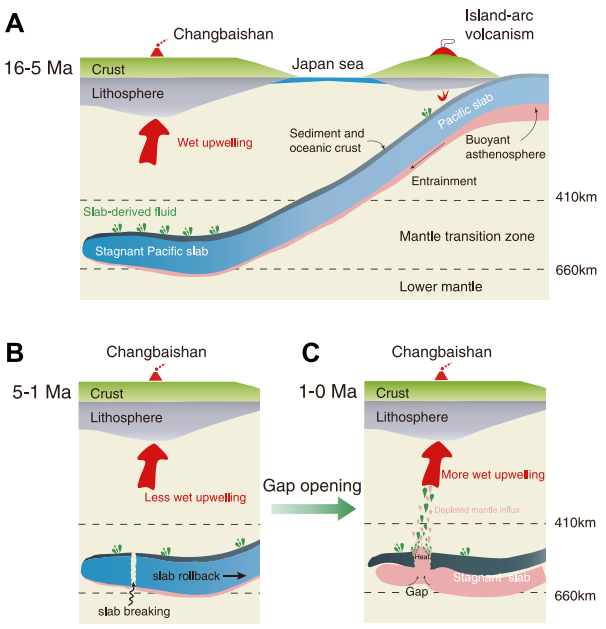

FIGURE 8
Schematic diagram illustrating our three-stage model for the genesis of the CBS volcanoes. **(A)** From 16 to 5 Ma. The Pacific Plate penetrates the mantle and stagnates in the mantle transition zone beneath the CBS volcanic region. Sub-slab asthenosphere is entrained downward. The buoyant and hydrous upwelling, induced by the dehydration of the stagnant Western Pacific slab, feeds the CBS volcanoes. **(B)** At about 5 Ma, slab breaking occurred, which caused partial removal of the slab and hence gradually weakened the influence of fluid. **(C)** From 1 Ma to present. A gap was created in the stagnant slab. The hot sub-slab asthenosphere melts went through the gap and heated the surrounding sediment and oceanic crust, providing fluid-rich and depleted mantle influx to the wet upwelling.

presence of hydrated partial melts beneath the stagnant slab has been confirmed by receiver functions (Liu et al., 2016b; Wang et al., 2020) and a recent 2D numerical simulation (Yang and Faccenda, 2020). Furthermore, the presence of a gap in the stagnant slab beneath the CBS is investigated by many seismic studies. Liu et al. (2015b) applied receiver function data to probe the MTZ structure beneath Northeast China. They found the uplift of the 660 km and lower velocity anomaly under the CBS area. Tao et al. (2018) performed a 3-D full waveform inversion using regional earthquakes data. They observed a thin low-velocity anomaly extending to the lower mantle inside the stagnant slab near the CBS, which was also imaged by Lai et al. (2019) using 2-D triplicated waveform modeling method. Kim et al. (2021) derived a 3-D S-wave velocity model of the upper mantle structure beneath East Asia using hundreds of thousands of relative traveltime residuals and found a low-velocity anomaly beneath CBS, which extends to the bottom of the MTZ through a slab gap in the stagnant Pacific slab. These results are almost identical to the structure detected by Tang et al. (2014). Very recently, Fan et al. (2021) imaged the MTZ structures beneath Northeast China using receiver function with Ps scattering kernel. The results shown that the 660-km discontinuity beneath the northwest of CBS is elevated by 5–15 km, which could be explained by the upwelling of high temperature materials. They suggested the upwelling may tear the stagnant slab. The uplift of 660-km discontinuity was also imaged by Liu et al. (2015b), Tian et al. (2016), and Zhang et al. (2016).

When there is a gap in the stagnant slab, the hot sub-lithospheric mantle melts could rise and provide the source of heat (Kuritani et al., 2017) to promote the release of fluid from surrounding sediment and oceanic crust, which gives rise to the enhancement of slab-derived fluid activity in the CBS basalts of 1–0 Ma ages (Figure 7A).

Regarding the variation of Sr-Nd isotopes, similar trend has been proposed by Tsung-jui Wu and Wu (2019) to delimit the time of Izanagi-Pacific ridge subduction. They examined the Sr-Nd isotopic values data of Cretaceous to Miocene igneous rocks within the Northeast Asian margin and found the decrease in $(^{87}Sr/^{86}Sr)_0$ and increase in $\varepsilon_{Nd(t)}$ after 56–46 Ma magmatic gap. They concluded that the asthenosphere beneath subducting slab entrained into the mantle wedge through the slab window, created by Izanagi-Pacific ridge subduction, leaded to the relatively depleted isotopic features in igneous rocks after 46 Ma. It is worth noting that the isotope changes they observed are greater than in this study, which could be due to the much larger gap caused by ridge subduction, allowing more depleted asthenosphere to pass. It may be possible that the depleted mantle component could also come from depleted upper mantle beneath the continents (Basu et al., 1991; Kuritani et al., 2009). In this case, the enhancement of fluid activity would lead to an increase in contribution of the depleted upper mantle. According to this causal relationship, the weakening of fluid influence for the CBS basalts of 5–1 Ma ages (Figure 7A) should result in a decrease in supplement of the upper mantle and a corresponding decrease of depleted features in basalts, which is contradictive to the almost constant Sr-Nd isotope values observed in Figures 7B,C. Alternatively, the weakened influence of fluid could be explained by the appearance of a gap within the stagnant slab. Gradual opening of the gap caused the local absence of the Pacific slab in the MTZ, which progressively reduced the fluid effect until the hot oceanic asthenosphere (Licheng et al., 2012; Wang et al., 2020; Yang and Faccenda, 2020) material rises through the gap and the influence of slab-derived fluid becomes stronger.

Through the above discussions, we propose a new three-stage dynamic model in generating the CBS volcanism (Figure 8). The western Pacific Plate, dragging sub-slab asthenosphere down, subducted in Japan Trench and became flattened in the MTZ at a depth of 410–660 km beneath Northeast China at ca. 16 Ma (Liu et al., 2017; Zhang et al., 2018). The dehydration of the stagnant slab induced the wet upwelling and generated the basalts above (Figure 8A). At ca. 5 Ma, a gap within the stagnant slab opened, which caused partial removal of the slab and hence gradually

weakened the influence of fluid (Figure 7A and Figure 8B). Until ca. 1 Ma, the buoyant hot and depleted sub-slab asthenosphere went through the gap and heated the surrounding sediment and oceanic crust, providing fluid-rich and depleted mantle influx to the wet upwelling, and finally generated the post-shield volcanism (Figure 8C). The existence of the recently formed gap may have caused the continuous recharge of mantle trachybasalt magma to crustal magma chamber (Fan et al., 2006) and triggered the "Millennium Eruption".

Following the geodynamic model proposed by Tang et al. (2014), Kuritani et al. (2017) argued that the oceanic asthenosphere materials beneath the stagnant Pacific slab just acted as a heat source, which made hydrous MTZ materials buoyant, but could not be the source for the CBS basalts because they lack the characteristics of ancient and/or recent subducted sediment components, which are the dominant geochemical aspects of the CBS basalts (Kuritani et al., 2011). Here we consider that sub-slab mantle is more likely to be part of the source components for the CBS basalts based on the synergistic changes between fluid activity and Sr-Nd isotopes.

Zhao and Tian (2013) proposed that large deep earthquakes (>500 km depth, magnitude >7.0) close to the CBS could release abundant fluids preserved in the faults within the slab to the overlying mantle wedge. The deep-earthquake related fluids may cause the more slab-derived fluid and relatively depleted basalts of 1–0 Ma ages found by the present study. According to this idea, the extra depleted component comes from the upper mantle, which is contrary to what we discussed above. A gap opening, however, is a more reasonable explanation for the temporal variation of slab-derived fluid activity and Sr-Nd isotopes.

The reasons for the slab window formation are yet uncertain. As discussed previously, it is unlikely that there is a deep mantle plume beneath the CBS area. Our observation that the influence of fluid is gradually weakened favors a gap opening in the stagnant Pacific slab. The trench retreat and rollback of the subducting slab caused breaking in the place where fractures or weak zones grew (Li et al., 2016; Lai et al., 2019). According to our suggested dynamic model, the age of the slab gap currently observed by tomography is about 5 Ma. The width of the gap is about 150 km (Tang et al., 2014), which is obtained from Figure 1C. Then the approximate rate for gap opening is estimated to be 3 cm/yr, close to the trench retreat velocity (2–5 cm/yr; Li et al., 2019; Miller et al., 2006) of the Pacific Plate.

Limitations

Basalts usually experience melt mixing and fractional crystallization before erupting to the Earth surface, which limits our ability to directly investigate the composition of source magma. In this study, rock samples are chosen with a fixed range of SiO_2 content (45–52 wt%) to avoid other rock types and reflect better the geochemical characteristics of the source magma.

Another drawback is the absence of basalts with ages from 10 to 5 Ma. As mentioned above, there is an eruption gap between the shield-forming stage (ca. 5–1 Ma) and pre-shield stage (ca. 23–10 Ma). We are therefore unable to collect samples from this period. More geological research is needed to study the gap of eruption.

Conclusion

Analyses of RF, PCA, and DNN results of global geochemical data of IAB and OIB show that the trained RF model could be applied to predict the degree of the basalt in the CBS area affected by slab-derived fluid. It is shown that the CBS basalts are highly influenced by fluid released from the stagnant slab. The effect of the fluid progressively weakens starting from ca. 5 Ma but begins to increase at ca. 1 Ma. After 1 Ma, the εNd(t) and $(^{87}Sr/^{86}Sr)_0$ values increase and decrease respectively. Based on these observations, it is inferred that the generation of the CBS basalts was controlled by the dehydration of stagnant Pacific slab and a gap within the stagnant slab opened at ca. 5 Ma making the partial removal of the slab and hence gradually weakening the influence of fluid. After 1 Ma, the hot sub-slab asthenosphere melts went through the gap and heated the surrounding sediment and oceanic crust, providing fluid-rich and depleted mantle components to the CBS basalts. The recently formed gap might indicate that the CBS volcanoes have a potential risk of eruption in the future.

Data availability statement

The datasets presented in this study can be found in online repositories. The names of the repository/repositories and accession number(s) can be found below: https://doi.org/10.5281/zenodo.5157656.

Author contributions

All authors listed have made a substantial, direct, and intellectual contribution to the work and approved it for publication.

Funding

The present work is supported by the Strategic Priority Research Program (B) of Chinese Academy of Sciences (Grant No. XDB18000000), the National Natural Science Foundation of China (Grant No. 12022517), and the Science and Technology Development Fund, Macau SAR (File No.

SKL-LPS(MUST)-2021-2023, 0005/2019/A1, 0048/2020/A1, and 0002/2019/APD).

Conflict of interest

The authors declare that the research was conducted in the absence of any commercial or financial relationships that could be construed as a potential.

Publisher's note

References

Aitchison, J. (1986), *The statistical analysis of compositional data*, 416 p. pp., Chapman & Hall, London ; New York.

Basu, A. R., Wang, J., Huang, W., Xie, G., and Tatsumoto, M. (1991). Major element, REE, and Pb, Nd and Sr isotopic geochemistry of cenozoic volcanic rocks of eastern China: Implications for their origin from suboceanic-type mantle reservoirs. *Earth Planet. Sci. Lett.* 105 (1), 149–169. doi:10.1016/0012-821x(91)90127-4

Brandmeier, M., and Wörner, G. (2016). Compositional variations of ignimbrite magmas in the central andes over the past 26 Ma—amultivariate statistical perspective. *Lithos* 262, 713–728. doi:10.1016/j.lithos.2016.07.011

Breiman, L., Friedman, J. H., Olshen, R. A., and Stone, C. J. (1999). *Classification and regression trees*. New York: CRC Press.

Breiman, L. (2001). Random forests. *Mach. Learn.* 45 (1), 5–32. doi:10.1023/A:1010933404324

Chen, Y., Zhang, Y., Graham, D., Su, S., and Deng, J. (2007). Geochemistry of Cenozoic basalts and mantle xenoliths in Northeast China. *Lithos* 96 (1), 108–126. doi:10.1016/j.lithos.2006.09.015

Choi, H.-O., Choi, S. H., Lee, Y. S., Ryu, J.-S., Lee, D.-C., Lee, S.-G., et al. (2020). Petrogenesis and mantle source characteristics of the late cenozoic baekdusan (changbaishan) basalts, North China craton. *Gondwana Res.* 78, 156–171. doi:10.1016/j.gr.2019.08.004

Chollet, F. (2015). *Keras*.

Di, Y., Tian, W., Chen, M., Li, Z., Chu, Z., and Liang, J. (2020). A method to estimate the pre-eruptive water content of basalts: Application to the Wudalianchi–Erkeshan–Keluo volcanic field, Northeastern China. *Am. Mineral.* 105 (2), 149–161. doi:10.2138/am-2020-7137

Fan, Q. C., Sui, J. L., Wang, T. H., Li, N., and Sun, Q. (2006). Eruption history and magma evolution of the trachybasalt in the Tianchi volcano, Changbaishan. *Acta Petrol. Sin.* 22 (6), 1449–1457.

Fan, Y., Han, Z., Juan, L. I., Xin, W., and QiFu, C. (2021). Topography of mantle transition zone discontinuities beneath Northeast China imaged by receiver function with Ps scattering kernel. *Chin. J. Geophys.* 64 (12), 4406–4424. doi:10.6038/cjg2021P0213

Fukao, Y., Obayashi, M., Nakakuki, T., Utada, H., Suetsugu, D., Irifune, T., et al. (2009). Stagnant slab : A review. *Annu. Rev. Earth Planet. Sci.* 37, 19–46. doi:10.1146/annurev.earth.36.031207.124224

GEOROC (2015). *Georoc: Geochemistry of rocks of the oceans and continents*. Available at: http://georoc.mpch-mainz.gwdg.de/georoc/.

Goodfellow, I., Bengio, Y., Courville, A., and Bengio, Y. (2016). *Deep learning*. Cambridge: MIT press.

Guo, X., and Yoshino, T. (2013). Electrical conductivity of dense hydrous magnesium silicates with implication for conductivity in the stagnant slab. *Earth Planet. Sci. Lett.* 369-370, 239–247. doi:10.1016/j.epsl.2013.03.026

Han, G., Li, J., Guo, G., Mooney, W. D., Karato, S.-i., and Yuen, D. A. (2020). Pervasive low-velocity layer atop the 410-km discontinuity beneath the northwest Pacific subduction zone: Implications for rheology and geodynamics. *Earth Planet. Sci. Lett.* 554, 116642. doi:10.1016/j.epsl.2020.116642

Hofmann, A. W., Jochum, K. P., Seufert, M., and White, W. M. (1986). Nb and Pb in oceanic basalts: New constraints on mantle evolution. *Earth Planet. Sci. Lett.* 79 (1), 33–45. doi:10.1016/0012-821x(86)90038-5

Honda, S., Morishige, M., and Orihashi, Y. (2007). Sinking hot anomaly trapped at the 410 km discontinuity near the Honshu subduction zone, Japan. *Earth Planet. Sci. Lett.* 261 (3-4), 565–577. doi:10.1016/j.epsl.2007.07.028

Huang, J., and Zhao, D. (2006). High-resolution mantle tomography of China and surrounding regions. *J. Geophys. Res.* 111 (9), B09305. doi:10.1029/2005jb004066

Karato, S.-i. (2011). Water distribution across the mantle transition zone and its implications for global material circulation. *Earth Planet. Sci. Lett.* 301 (3), 413–423. doi:10.1016/j.epsl.2010.11.038

Kelbert, A., Schultz, A., and Egbert, G. (2009). Global electromagnetic induction constraints on transition-zone water content variations. *Nature* 460, 1003–1006. doi:10.1038/nature08257

Kim, Y.-W., Chang, S.-J., Witek, M., Ning, J., and Wen, J. (2021). S-velocity mantle structure of East Asia from teleseismic traveltime tomography: Inferred mechanisms for the cenozoic intraplate volcanoes. *J. Geophys. Res. Solid Earth* 126 (3), e2020JB020345. doi:10.1029/2020JB020345

Kingma, D. P., and Ba, J. (2014). *Adam: A method for stochastic optimization*. *arXiv preprint arXiv:*1412.6980.

Kohavi, R. (1995). *Proceedings of the 14th international joint conference on artificial intelligence*. Montreal, Quebec: Canada.

Kuritani, T., Ohtani, E., and Kimura, J.-I. (2011). Intensive hydration of the mantle transition zone beneath China caused by ancient slab stagnation. *Nat. Geosci.* 4, 713–716. doi:10.1038/ngeo1250

Kuritani, T., Sakuyama, T., Kamada, N., Yokoyama, T., and Nakagawa, M. (2017). Fluid-fluxed melting of mantle versus decompression melting of hydrous mantle plume as the cause of intraplate magmatism over a stagnant slab: Implications from Fukue Volcano Group, SW Japan. *Lithos* 282-283, 98–110. doi:10.1016/j.lithos.2017.02.011

Kuritani, T., Xia, Q.-K., Kimura, J.-I., Liu, J., Shimizu, K., Ushikubo, T., et al. (2019). Buoyant hydrous mantle plume from the mantle transition zone. *Sci. Rep.* 9 (1), 6549. doi:10.1038/s41598-019-43103-y

Kuritani, T., Kimura, J.-I., Miyamoto, T., Wei, H., Shimano, T., Maeno, F., et al. (2009). Intraplate magmatism related to deceleration of upwelling asthenospheric mantle: Implications from the Changbaishan shield basalts, northeast China. *Lithos* 112 (3), 247–258. doi:10.1016/j.lithos.2009.02.007

Lai, Y., Chen, L., Wang, T., and Zhan, Z. (2019). Mantle transition zone structure beneath Northeast Asia from 2-D triplicated waveform modeling: Implication for a segmented stagnant slab. *J. Geophys. Res. Solid Earth* 124 (2), 1871–1888. doi:10.1029/2018jb016642

LeCun, Y., Bengio, Y., and Hinton, G. (2015). Deep learning. *Nature* 521, 436–444. doi:10.1038/nature14539

Li, J., Tosi, N., Maierová, P., and Yuen, D. A. (2016). *Evidence from caustic waveform modeling for long slab thickening above the 660-km discontinuity under Northeast Asia: Dynamic implications*, 211. Washington, DC: American Geophysical Union, 5–18.

Li, S.-G., Yang, W., Ke, S., Meng, X., Tian, H., Xu, L., et al. (2017). Deep carbon cycles constrained by a large-scale mantle Mg isotope anomaly in eastern China. *Natl. Sci. Rev.* 4 (1), 111–120. doi:10.1093/nsr/nww070

Li, S., Weng, A., Li, J., Shan, X., Han, J., Tang, Y., et al. (2020). Deep origin of Cenozoic volcanoes in Northeast China revealed by 3-D electrical structure. *Sci. China Earth Sci.* 63 (4), 533–547. doi:10.1007/s11430-018-9537-2

Li, Z.-H., Gerya, T., and Connolly, J. A. D. (2019). Variability of subducting slab morphologies in the mantle transition zone: Insight from petrological-thermomechanical modeling. *Earth-Science Rev.* 196, 102874. doi:10.1016/j.earscirev.2019.05.018

LiCheng, J.-h., Shi, J.-y., and Huang, F. (2012). *Brief introduction of back propagation (BP) neural network algorithm and its improvement, paper*

presented at advances in computer science and information engineering. Berlin, Heidelberg: Springer Berlin Heidelberg.

Liu, J., Han, J., and Fyfe, W. S. (2001). Cenozoic episodic volcanism and continental rifting in northeast China and possible link to Japan Sea development as revealed from K–Ar geochronology. *Tectonophysics* 339 (3), 385–401. doi:10.1016/s0040-1951(01)00132-9

Liu, J. Q., Chen, S. S., Guo, W. F., Sun, Q., Zhang, M., and Guo, Z. (2015a). Research advances in the Mt. Changbai volcano. *Bull. Mineral. Pet. Geochem* 34, 710–723.

Liu, L., and Zhou, Q. (2015). Deep recycling of oceanic asthenosphere material during subduction. *Geophys. Res. Lett.* 42 (7), 2204–2211. doi:10.1002/2015gl063633

Liu, S.-A., Wang, Z.-Z., Li, S.-G., Huang, J., and Yang, W. (2016a). Zinc isotope evidence for a large-scale carbonated mantle beneath eastern China. *Earth Planet. Sci. Lett.* 444, 169–178. doi:10.1016/j.epsl.2016.03.051

Liu, X., Zhao, D., Li, S., and Wei, W. (2017). Age of the subducting Pacific slab beneath East Asia and its geodynamic implications. *Earth Planet. Sci. Lett.* 464, 166–174. doi:10.1016/j.epsl.2017.02.024

Liu, Z., Niu, F., Chen, Y. J., Grand, S., Kawakatsu, H., Ning, J., et al. (2015b). Receiver function images of the mantle transition zone beneath NE China: New constraints on intraplate volcanism, deep subduction and their potential link. *Earth Planet. Sci. Lett.* 412, 101–111. doi:10.1016/j.epsl.2014.12.019

Liu, Z., Park, J., and Karato, S. i. (2016b). Seismological detection of low-velocity anomalies surrounding the mantle transition zone in Japan subduction zone. *Geophys. Res. Lett.* 43 (6), 2480–2487. doi:10.1002/2015gl067097

Long, M. D., and Silver, P. G. (2008). The subduction zone flow field from seismic anisotropy: A global view. *Science* 319 (5861), 315–318. doi:10.1126/science.1150809

Louppe, G., Wehenkel, L., Sutera, A., and Geurts, P. (2013). *Advances in neural information processing systems*. Understanding variable importances in forests of randomized trees.

McCulloch, M. T., and Gamble, J. A. (1991). Geochemical and geodynamical constraints on subduction zone magmatism. *Earth Planet. Sci. Lett.* 102 (3), 358–374. doi:10.1016/0012-821x(91)90029-h

Middlemost, E. A. K. (1994). Naming materials in the magma/igneous rock system. *Earth-Science Rev.* 37 (3-4), 215–224. doi:10.1016/0012-8252(94)90029-9

Miller, M. S., Kennett, B. L. N., and Toy, V. G. (2006). Spatial and temporal evolution of the subducting Pacific plate structure along the Western Pacific margin. *J. Geophys. Res.* 111 (2). doi:10.1029/2005JB003705

Morishige, M., Honda, S., and Yoshida, M. (2010). Possibility of hot anomaly in the sub-slab mantle as an origin of low seismic velocity anomaly under the subducting Pacific plate. *Phys. Earth Planet. Interiors* 183 (1-2), 353–365. doi:10.1016/j.pepi.2010.04.002

Obayashi, M., Yoshimitsu, J., Nolet, G., Fukao, Y., Shiobara, H., Sugioka, H., et al. (2013). Finite frequency whole mantle P wave tomography: Improvement of subducted slab images. *Geophys. Res. Lett.* 40 (21), 5652–5657. doi:10.1002/2013gl057401

Pearce, J. A., and Peate, D. W. (1995). Tectonic implications of the composition of volcanic arc magmas. *Annu. Rev. Earth Planet. Sci.* 23 (1), 251–285. doi:10.1146/annurev.ea.23.050195.001343

Pedregosa, F., Varoquaux, G., Gramfort, A., Michel, V., Thirion, B., Grisel, O., et al. (2011). Scikit-learn: Machine learning in Python. *J. Mach. Learn. Res.* 12, 2825–2830.

Phipps Morgan, J., Hasenclever, J., Hort, M., Rüpke, L., and Parmentier, E. (2007). On subducting slab entrainment of buoyant asthenosphere. *Terra nova.* 19 (3), 167–173. doi:10.1111/j.1365-3121.2007.00737.x

Rudnick, R. L., and Gao, S. (2014). "4.1 - composition of the continental crust," in *Treatise on Geochemistry*. Editors H. D. Holland and K. K. Turekian Second Edition (Oxford: Elsevier), 1–51.

Shore, J., and Johnson, R. (1980). Axiomatic derivation of the principle of maximum entropy and the principle of minimum cross-entropy. *IEEE Trans. Inf. Theory* 26 (1), 26–37. doi:10.1109/tit.1980.1056144

Song, T. R. A., and Kawakatsu, H. (2012). Subduction of oceanic asthenosphere: Evidence from sub-slab seismic anisotropy. *Geophys. Res. Lett.* 39 (17). doi:10.1029/2012gl052639

Srivastava, N., Hinton, G., Krizhevsky, A., Sutskever, I., and Salakhutdinov, R. (2014). Dropout: A simple way to prevent neural networks from overfitting. *J. Mach. Learn. Res.* 15 (1), 1929–1958.

Tang, Y., Obayashi, M., Niu, F., Grand, S. P., Chen, Y. J., Kawakatsu, H., et al. (2014). Changbaishan volcanism in northeast China linked to subduction-induced mantle upwelling. *Nat. Geosci.* 7 (6), 470–475. doi:10.1038/ngeo2166

Tao, K., Grand, S. P., and Niu, F. (2018). Seismic structure of the upper mantle beneath eastern Asia from full waveform seismic tomography. *Geochem. Geophys. Geosyst.* 19 (8), 2732–2763. doi:10.1029/2018gc007460

Tian, Y., Zhu, H., Zhao, D., Liu, C., Feng, X., Liu, T., et al. (2016). Mantle transition zone structure beneath the Changbai volcano: Insight into deep slab dehydration and hot upwelling near the 410 km discontinuity. *J. Geophys. Res. Solid Earth* 121 (8), 5794–5808. doi:10.1002/2016jb012959

Tsung-Jui Wu, J., and Wu, J. (2019). Izanagi-Pacific ridge subduction revealed by a 56 to 46 Ma magmatic gap along the northeast Asian margin. *Geology* 47 (10), 953–957. doi:10.1130/G46778.1

Uieda, L., Tian, D., Leong, W. J., Jones, M., Schlitzer, W., Toney, L., et al. (2021). *PyGMT: A Python interface for the generic mapping tools*. Zenodo, doi:10.5281/zenodo.5607255

Wang, X., Chen, Q.-F., Niu, F., Wei, S., Ning, J., Li, J., et al. (2020). Distinct slab interfaces imaged within the mantle transition zone. *Nat. Geosci.* 13, 822–827. doi:10.1038/s41561-020-00653-5

Wang, X.-C., Wilde, S. A., Li, Q.-L., and Yang, Y.-N. (2015). Continental flood basalts derived from the hydrous mantle transition zone. *Nat. Commun.* 6 (1), 7700. doi:10.1038/ncomms8700

Wei, H., Liu, G., and Gill, J. (2013). Review of eruptive activity at tianchi volcano, changbaishan, Northeast China: Implications for possible future eruptions. *Bull. Volcanol.* 75 (4), 706. doi:10.1007/s00445-013-0706-5

Wei, H., Sparks, R. S. J., Liu, R., Fan, Q., Wang, Y., Hong, H., et al. (2003). Three active volcanoes in China and their hazards. *J. Asian Earth Sci.* 21 (5), 515–526. doi:10.1016/s1367-9120(02)00081-0

Yang, J., and Faccenda, M. (2020). Intraplate volcanism originating from upwelling hydrous mantle transition zone. *Nature* 579 (7797), 88–91. doi:10.1038/s41586-020-2045-y

Yu, S.-Y., Xu, Y.-G., Zhou, S.-H., Lan, J.-B., Chen, L.-M., Shen, N.-P., et al. (2018). Late Cenozoic basaltic lavas from the Changbaishan-Baoqing Volcanic Belt, NE China: Products of lithosphere-asthenosphere interaction induced by subduction of the Pacific plate. *J. Asian Earth Sci.* 164, 260–273. doi:10.1016/j.jseaes.2018.06.031

Zhang, M., Guo, Z., Liu, J., Liu, G., Zhang, L., Lei, M., et al. (2018). The intraplate changbaishan volcanic field (China/North Korea): A review on eruptive history, magma Genesis, geodynamic significance, recent dynamics and potential hazards. *Earth-Science Rev.* 187, 19–52. doi:10.1016/j.earscirev.2018.07.011

Zhang, R., Gao, Z., Wu, Q., Xie, Z., and Zhang, G. (2016). Seismic images of the mantle transition zone beneath Northeast China and the Sino-Korean craton from P-wave receiver functions. *Tectonophysics* 675, 159–167. doi:10.1016/j.tecto.2016.03.002

Zhao, D., and Tian, Y. (2013). Changbai intraplate volcanism and deep earthquakes in East Asia: A possible link? *Geophys. J. Int.* 195 (2), 706–724. doi:10.1093/gji/ggt289

Zhao, D., Tian, Y., Lei, J., Liu, L., and Zheng, S. (2009). Seismic image and origin of the Changbai intraplate volcano in East Asia: Role of big mantle wedge above the stagnant Pacific slab. *Phys. Earth Planet. Interiors* 173 (3), 197–206. doi:10.1016/j.pepi.2008.11.009

Zhao, Y., Zhang, Y., Geng, M., Jiang, J., and Zou, X. (2019). Involvement of slab-derived fluid in the generation of cenozoic basalts in Northeast China inferred from machine learning. *Geophys. Res. Lett.* 46 (10), 5234–5242. doi:10.1029/2019GL082322

Zindler, A., and Hart, S. (1986). Chemical geodynamics. *Annu. Rev. Earth Planet. Sci.* 14, 493–571. doi:10.1146/annurev.ea.14.050186.002425

Zou, H., Fan, Q., and Yao, Y. (2008). U–Th systematics of dispersed young volcanoes in NE China: Asthenosphere upwelling caused by piling up and upward thickening of stagnant pacific slab. *Chem. Geol.* 255 (1), 134–142. doi:10.1016/j.chemgeo.2008.06.022